Revealing a Correlation between Structure and *in vitro* activity of mRNA Lipid Nanoparticles

Xiaoxia Chen[1,2], Mengrong Li[1,2], Fan Jiang[1,2], Liang Hong[1,2,3,4,5,*], and Zhuo Liu[2,3,4,5,*]

[1]School of Physics and Astronomy, Shanghai Jiao Tong University, Shanghai 200240, China.

[2]Institute of Natural Sciences, Shanghai Jiao Tong University, Shanghai 200240, China.

[3]Shanghai National Centre for Applied Mathematics (SJTU Center), MOE-LSC, Shanghai Jiao Tong University, Shanghai 200240, China.

[4]Zhangjiang Institute for Advanced Study, Shanghai Jiao Tong University, Shanghai 201203, China.

[5]Shanghai Artificial Intelligence Laboratory, Shanghai 200232, China.

*e-mail: judeliu@sjtu.edu.cn and hongl3liang@sjtu.edu.cn

Abstract

Messenger RNA-containing lipid nanoparticles (mRNA-LNPs) represent a promising platform for disease prevention, cancer immunotherapy, and gene editing, etc. Despite the clinical success of mRNA-LNPs based vaccines in preventing infectious diseases, the relationship between their structure and efficacy remains poorly understood, primarily due to their complex chemical composition. In this study, we generated a series of mRNA-LNPs with varied structural properties and *in vitro* cellular activities by altering their processing and storage conditions to investigate the structure-activity relationship (SAR) of these nanoparticles. Our findings revealed a moderate anticorrelation between particle size distribution and *in vitro* activity, while nanoparticle size and morphology exhibited only weak correlations with efficacy. Notably, the intensity of a characteristic peak, as detected by small angle X-ray scattering (SAXS), demonstrated a strong correlation with *in vitro* activity. Additionally, the peak width and area were moderately correlated and anticorrelated with activity, respectively. These observations suggest that a more ordered internal structure, as identified by SAXS, is likely associated with enhanced *in vitro* activity of mRNA-LNPs. Further analysis using ^{31}P nuclear magnetic resonance indicated that lyophilization may induce phase separation of mRNA and lipids within the LNPs, leading to a diminished SAXS peak and reduced *in vitro* activity. Overall, our study establishes an SAR for mRNA-LNPs, highlighting that a more ordered internal structure correlates with higher efficacy, which could be instrumental in high-throughput screening of LNP libraries for mRNA loading and monitoring efficacy during storage.

Significance

In addition to the two mRNA-based vaccines developed for COVID-19, the FDA approved a third mRNA-based vaccine for respiratory syncytial virus in 2024. These vaccines rely on

mRNA-containing lipid nanoparticles (mRNA-LNPs), which are also being explored for cancer treatment, gene editing, and antibody production. Despite their promise, the structure-activity relationship of mRNA-LNPs remains inadequately understood, limiting the optimization of lipid formulations, long-term storage, and mechanistic insights. Our study suggests that an ordered internal structure correlates with enhanced *in vitro* efficacy, consistent with previous findings. We identified the intensity of a peak at ~0.13 $Å^{-1}$ in small-angle X-ray scattering (SAXS) as a strong indicator of the efficacy. Furthermore, we demonstrated that this correlation aroused from phase separation between mRNA and lipids inside LNPs in the lyophilization process. These insights offer a straightforward method to predict *in vitro* activity of mRNA-LNPs with certain formulation and shed light on the mechanisms underlying the loss of mRNA-LNPs' activity during lyophilization.

Introduction

The emergency use authorizations of two mRNA-based COVID-19 vaccines in 2020 (1, 2) garnered significant attention from both the academic and industrial community. These vaccines employ mRNA-containing lipid nanoparticles (mRNA-LNPs), where the mRNA encodes the viral spike protein, prompting an immune response (3). This vaccination strategy builds on the success of LNPs in gene therapy and lipophilic drug delivery, which utilize ionizable lipids, helper phospholipids, cholesterol, and polyethylene glycol-lipids (PEG-lipids) (4). Beyond infectious diseases, mRNA-LNPs hold promise for cancer immunotherapy, protein replacement therapy, and *in vivo* gene editing (5, 6). In June 2024, the FDA approved Moderna's mRNA-based respiratory syncytial virus vaccine, mRNA-1345, marking the third mRNA-LNP vaccine to reach the market, further validating the potential of mRNA-LNPs in immunotherapy (7).

Despite these exciting successes in application, the structure-activity relationship (SAR) of mRNA-LNPs remains incompletely understood, hindering their rational design and further optimization. This gap highlights the need for an efficient approach to high-throughput screening of mRNA-LNP formulations based on nanoparticle structure. Researchers have attempted to bridge the gap between nanoparticle structure and transfection potency using advanced techniques such as cryogenic electron microscopy (cryo-EM) (8, 9), small angle neutron scattering (SANS) (10, 11), and small angle X-ray scattering (SAXS) (12-15). Although cryo-EM and SANS offer high-resolution insights into morphology, lipid distribution, and internal structure, their complexity and time-consumption of sample preparation prevent them from being applied in high-throughput experiments (9, 10, 16-20). In contrast, synchrotron SAXS allows for structural analysis with simple sample preparation and rapid data collection, making it more practical for SAR investigations (12-15). Owing to only one or two peaks at ~0.1 $Å^{-1}$ can be distinguished while probing the mRNA-LNPs by SAXS (10, 16, 18),

previous studies have primarily focused on core structures (12, 13, 15) or introduced structure-forming helper lipids (12-14) to enrich structural information. However, changes in the shell structure have also been reported to influence mRNA-LNP efficacy (9-11, 16). Additionally, the use of structure-forming helper lipids may obscure a direct understanding of the SAR. Therefore, there is a pressing need for *in situ* investigations of mRNA-LNP SAR without external interference to achieve a deeper understanding.

In this work, we prepared 58 mRNA-LNP samples with varying *in vitro* cellular activities by manipulating processing and storage conditions. To explore the relationship between structure and activity, we assessed key structural parameters, including encapsulation efficiency (EE%), hydrodynamic radius (R_h), radius of gyration (R_g), and the degree of internal structural order. The *in vitro* activity of each mRNA-LNP sample was quantified by normalizing luminescence to the amount of encapsulated mRNA during transfection. We observed a strong correlation between the intensity of a SAXS peak at ~0.13 $Å^{-1}$ and in *vitro* activity, with the peak width and area showing moderate positive and negative correlations, respectively. These findings suggest that an ordered internal structure, as indicated by SAXS, enhances mRNA-LNP efficacy. Further ^{31}P Nuclear Magnetic Resonance (NMR) analysis confirmed that lyophilization may induce phase separation in the core of mRNA-LNPs, leading to a weakened SAXS peak and reduced activity. Additionally, particle size distribution exhibited a moderate anticorrelation with activity, while other structural features showed minimal correlation. Our results establish a structure-activity relationship (SAR) for mRNA-LNPs, indicating that a more ordered internal structure may contribute to higher efficacy. This insight could be valuable for high-throughput screening of LNP libraries for mRNA loading and for monitoring efficacy of certain lipids formulation during processing and storage.

Results

Preparing the mRNA-LNP samples with varied *in vitro* activity

To elucidate the SAR of mRNA-LNPs, it is essential to generate a series of mRNA-LNPs with diverse structural characteristics and *in vitro* cellular efficacy. Previous studies have demonstrated that processing and storage conditions significantly impact both the structure and efficacy of mRNA-LNPs (17, 21). Accordingly, we prepared 58 distinct mRNA-LNP samples by varying their processing and storage conditions. Detailed methods for sample preparation are provided in the Materials and Methods, and a comprehensive list of sample information is available in Table S1 of the Supporting Information (SI). The samples were subjected to freezing or lyophilization under different buffer compositions, lyoprotectants, and storage conditions, while maintaining an identical chemical composition. Given that lyophilization can induce changes in morphology and structure (17, 21), we anticipated sampling a broader structural spectrum.

The mRNA used in our study, encoding an enhanced green fluorescent protein (eGFP) linked to firefly luciferase (fLuc) with length of 2,856 nucleotides (nt). The *in vitro* transfection efficacy of the 58 mRNA-LNP samples was assessed in human embryonic kidney 293 cells transformed with sheared simian virus 40 large T antigen (HEK293T). We quantified fLuc expression by measuring luminescence and normalized these values to the amount of encapsulated mRNA in each sample to evaluate transfection potency. As depicted in Figure 1, variations in sample preparation methods led to distinct normalized luminescence (Norm Lumi). This wide distribution of Norm Lumi values provided a robust dataset for examining the factors influencing the *in vitro* activity of mRNA-LNPs.

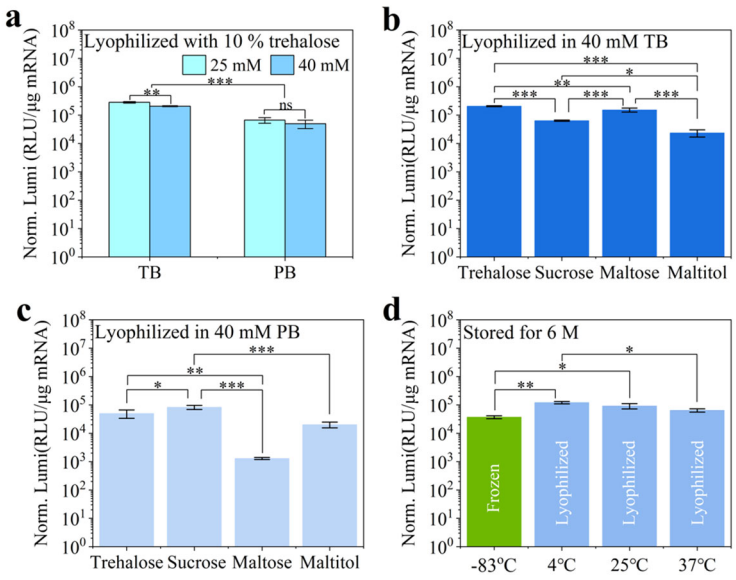

Figure 1. Normalized luminescence (Norm Lumi) of mRNA-LNPs in HEK293T cells. (a) Norm Lumi of mRNA-LNPs lyophilized with 10% (w/v) trehalose in 25 mM Tris Buffer (TB) and Sodium Phosphorate Buffer (PB) colored in cyan, and in 40 mM Tris Buffer (TB) and Sodium Phosphorate Buffer (PB) colored in blue. (b) Norm Lumi of mRNA-LNPs lyophilized in 40 mM Tris Buffer (TB) with 10% (w/v) lyoprotectants, including trehalose, sucrose, maltose, and maltitol. (c) Norm Lumi of mRNA-LNPs lyophilized in 40 mM Sodium Phosphorate Buffer (PB) with 10% (w/v) lyoprotectants, including trehalose, sucrose, maltose, and maltitol. (d) Norm Lumi of frozen mRNA-LNPs at -83 °C stored for six months (6 M) colored in blue, and Norm Lumi of lyophilized mRNA-LNPs stored at 4, 25, and 37 °C for 6 M colored in green. *, **, and *** refer to $p \leqslant 0.05$, $p \leqslant 0.01$, and $p \leqslant 0.001$, respectively. Pairs marked ns in (a) represents not significant, while those in (c) and (d) were not labeled.

Morphology characterizations for the mRNA-LNP samples

To investigate the relationship between the structure of mRNA-LNPs and their *in vitro* activity, we first analyzed their morphology and particle size distribution. As illustrated in Figure 2a, mRNA-LNPs predominantly exhibit a spherical morphology when a fishbone chip is used in

the microfluidics process. However, when the fishbone chip is replaced with a Tesla chip, the morphology shifts to predominantly bleb structures (Figure 2b). Notably, mRNA-LNPs with bleb structures demonstrated higher *in vitro* mRNA transfection efficacy (Figure 2c), consistent with findings reported by Cheng et al. (8). This outcome indicates that our sample preparation methods can yield mRNA-LNPs with variations in both morphology and *in vitro* activity. Additionally, the morphological differences among mRNA-LNPs can be quantified by the ratio of the radius of gyration (R_g) to the hydrodynamic radius (R_h) (Figure 2d). Using dynamic light scattering (DLS), we observed that particle size exhibited minimal correlation with *in vitro* activity (Figure 2e). However, the polydispersity index (PdI), reflecting particle size distribution, showed a moderate inverse correlation with protein expression in HEK293T cells (Figure 2f).

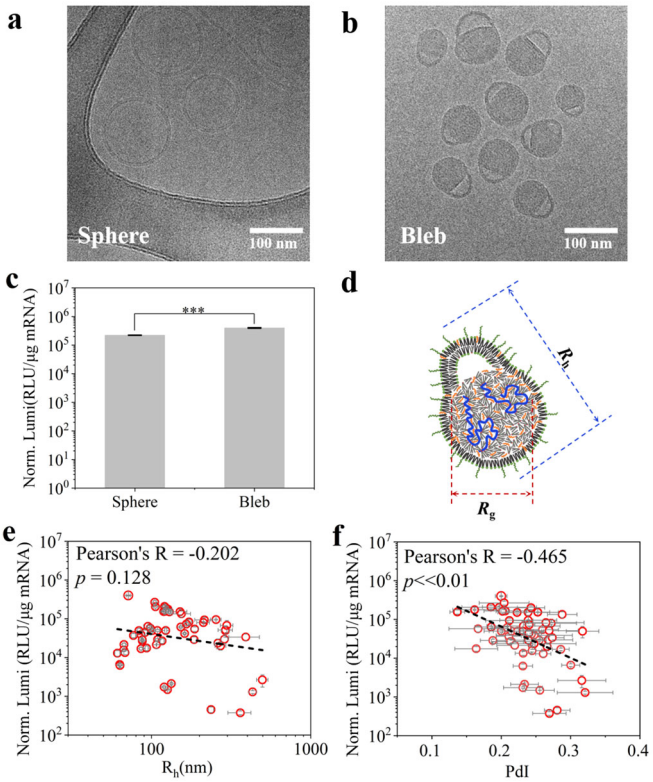

Figure 2. Morphology characterizations for the mRNA-LNP samples. (a) Cryo-EM image of mRNA-LNPs predominantly exhibiting spherical structures. (b) Cryo-EM image of mRNA-LNPs primarily displaying bleb structures. (c) Normalized luminescence (Norm Lumi) of the

mRNA-LNPs shown in panels a and b, where *** refers to $p \leqslant 0.001$. (d) Schematic representation of an mRNA-LNP with bleb morphology, where R_h and R_g denote hydrodynamic radius and radius of gyration, respectively. (e) Norm Lumi of mRNA-LNPs plotted as a function of their hydrodynamic radius (R_h). (f) Norm Lumi of mRNA-LNPs as a function of their polydispersity index (PdI), both characterized using DLS. Dash lines represent linear fits to the data.

Structural characterizations for the mRNA-LNP samples by SAXS

Given the lack of significant correlation between morphology and *in vitro* activity, we extended our analysis to the internal structure of mRNA-LNPs, which has been reported to influence their delivery efficiency (9, 11, 12, 14, 15, 22). Notably, mRNA-LNPs with ordered internal structures, as revealed by SAXS, have been associated with enhanced intracellular mRNA delivery compared to those with disordered cores (9, 12, 14, 22). To examine these structural variations, we employed SAXS to analyze both drug-free LNPs and mRNA-LNPs.

Figure 3a shows a distinct peak at ~0.13 $Å^{-1}$ in the SAXS curve of mRNA-LNPs, indicating an ordered structure, whereas this peak is absent in drug-free LNPs. The SAXS data for the drug-free LNPs were fitted using a generic broad peak model constituted by a Porod curve and a Lorentz peak (Figure 3b, Table S2). For the mRNA-LNPs, the SAXS curve was fitted with a linear combination of this broad peak model, with the peak position fixed from the drug-free LNP fitting, and an additional Gaussian peak, allowing all parameters to vary (Figure 3c and 3d). Detailed methods and results for the data fitting are provided in Materials and Methods and the SI (Figure S1, Tables S2 and S3). This approach enabled us to resolve multiple structural features, including the intensity, width, and area of the Gaussian peak, the area of the Lorentz peak derived from the broad peak model for drug-free LNPs, and the ratio of Gaussian to Lorentz peak areas. It should be noted that 18 out of 58 samples exhibited little Gaussian

peak in their SAXS curves and showed negligible activity. Thus 40 samples with a prominent peak at ~0.13 $Å^{-1}$ were used for further analysis.

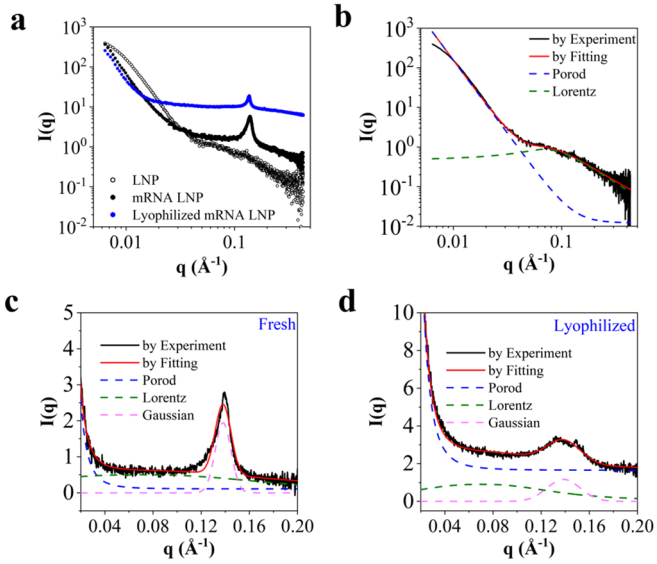

Figure 3. Structural characterizations for drug-free LNPs and mRNA-LNPs. (a) SAXS profiles of drug-free LNPs (black circles), fresh mRNA-LNPs (black dots), and lyophilized mRNA-LNPs (blue dots). (b) SAXS data for drug-free LNPs were fitted using a broad peak model. (c) SAXS data for fresh mRNA-LNPs were fitted with a broad peak model and a Gaussian peak. (d) SAXS data for lyophilized mRNA-LNPs with 15% (w/v) trehalose, stored at 25 °C for 12 weeks, were also fitted using the same model. In panels b-d, the blue, green, and pink dashed lines represent the Porod scaling law, Lorentz peak, and Gaussian peak, respectively, while the solid black and red lines correspond to experimental and fitting results.

Correlation between structure and *in vitro* activity of mRNA-LNPs

The morphology of mRNA-LNPs was characterized by capturing metrics such as hydrodynamic radius (R_h), polydispersity index (PdI), and cryo-EM images. SAXS further provided insights into structural features, including R_g, R_g/R_h ratios, and the subsequent fitting parameters of the peak at ~0.13 $Å^{-1}$. To elucidate the relationship between these structural

indices and the *in vitro* activity of 40 mRNA-LNP samples, we calculated Pearson correlation coefficients.

Our analysis, presented in Figure 4, demonstrates a strong positive correlation (Pearson coefficient up to 0.88) between *in vitro* activity and the intensity of the Gaussian peak from SAXS fitting. In addition, the width and area of the Gaussian peak show moderate negative and positive correlations with activity, respectively (Figure 4c and 4d). These findings suggest that mRNA-LNPs with higher peak intensity, narrower width, and larger area—indicative of a more ordered internal structure—are more likely to exhibit enhanced *in vitro* efficacy (18). Conversely, the area of the Lorentz peak, associated with disordered structures, shows minimal correlation with activity, as do R_g, R_h, R_g/R_h ratios, and the Lorentz-to-Gaussian peak area ratio (Figures 4 and S2). This implies that *in vitro* activity is largely independent of size, morphology, and disordered structures within mRNA-LNPs. Besides, PdI exhibits a moderate inverse correlation with *in vitro* activity (Figures 4 and S2b), consistent with the trends observed across all 58 samples (Figure 2f).

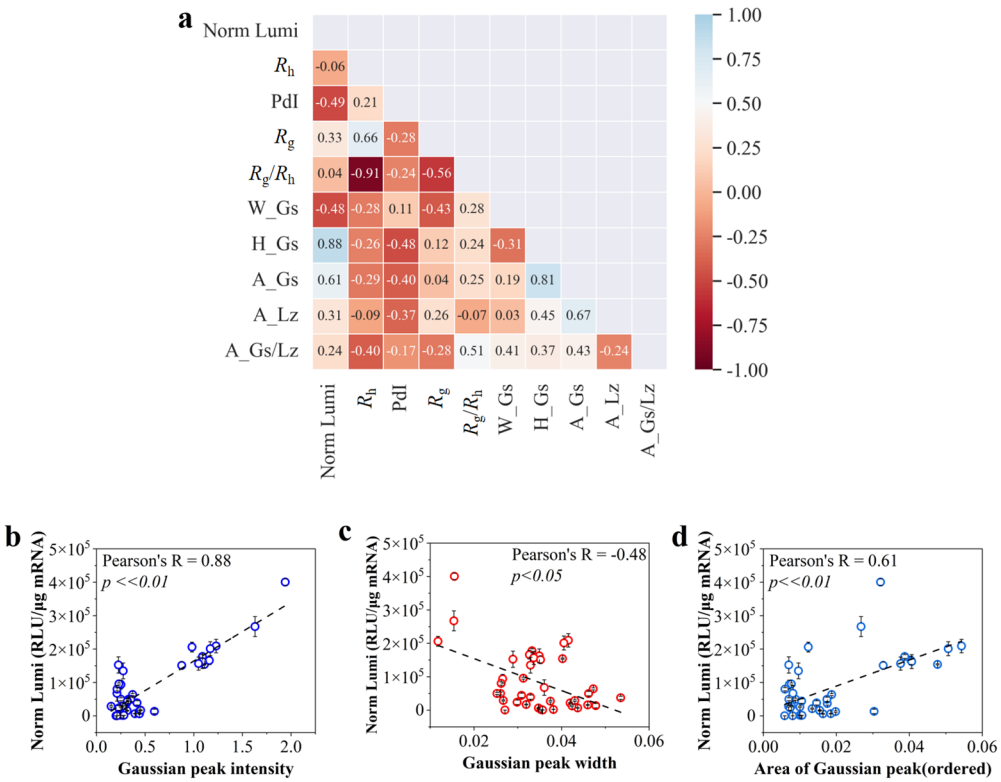

Figure 4. Correlation between structural indices and *in vitro* activity of mRNA-LNPs. (a) The correlation between structural indices and the *in vitro* activity of mRNA-LNPs is depicted through color-coded heat maps, which rank the indices according to their Pearson correlation coefficients. The parameters R_g, R_h, and PdI represent the radius of gyration, hydrodynamic radius, and polydispersity index of mRNA-LNPs, respectively. W_Gs, H_Gs, and A_Gs correspond to the width, intensity, and area of the Gaussian peak derived from fitting the SAXS peak at ~0.13 $Å^{-1}$, while A_Lz refers to the area of the Lorentz peak. The *in vitro* activity of mRNA-LNPs is expressed as Norm Lumi, which represents the luminescence intensity of expressed fLuc normalized by the amount of encapsulated mRNA in LNPs. Norm Lumi of mRNA-LNPs as a function of (b) intensity, (c) width, and (d) area of the Gaussian peak obtained from fitting the SAXS curves.

Discussion

Despite the recognized importance of the structure of mRNA-LNPs in determining bioactivity, the SAR remains poorly understood, largely due to limited resources and the complexity of structural characterization. This gap in understanding hinders the accurate prediction of bioactivity of mRNA-LNPs. To address this challenge, we prepared 58 mRNA-LNP samples with varying structures and *in vitro* activities through freezing and freeze-drying. Structural characterization was performed using SAXS, revealing that only 40 samples exhibited a characteristic peak at ~0.13 $Å^{-1}$ in SAXS analysis. Furthermore, we calculated Pearson correlation coefficients between structural parameters and *in vitro* activity for these 40 samples, with activity quantified by luminescence intensity of expressed fLuc normalized to the amount of transfected mRNA which was encapsulated in LNP. This approach ensured that activity measurements were independent of encapsulation efficiency. It is noteworthy that the intensity of the Gaussian peak derived from SAXS data showed a strong correlation with *in vitro* activity,

while the area and width of the Gaussian peak were moderately correlated and anticorrelated with activity, respectively (Figure 4b-d). This finding offers a reliable index—the intensity of the characteristic Gaussian peak—for predicting mRNA-LNPs' bioactivity and facilitates high-throughput screening of LNP formulations using SAXS.

In addition to developing a methodology to correlate the SAR of mRNA-LNPs, we sought to understand the mechanisms underlying the loss of efficacy in mRNA-LNPs following lyophilization. Previous studies have indicated that the SAXS peak at ~0.1 $Å^{-1}$ is prominent only when mRNA is encapsulated within LNPs (10, 19). We propose that this SAXS peak originates from the periodic repeating distances between structural units formed by mRNA and adjacent ionizable lipids, consistent with prior SAXS (10) and SANS (16) findings. The high intensity, narrow width, and large area of the SAXS peak at ~0.13 $Å^{-1}$ suggest an ordered periodic distance of approximately 5 nm, indicating a more ordered internal structure, which is likely associated with higher *in vitro* activity (see Figure 4). After lyophilization and reconstitution, the mRNA-LNPs may adopt a bleb morphology characterized by water compartments containing mRNA molecules separate from lipid compartments, similar to the morphology observed in self-amplifying mRNA-LNPs (19). This separation likely results in a disordered internal structure, evidenced by a lower intensity Gaussian peak at ~0.13 $Å^{-1}$ in SAXS analysis, which correlates with diminished *in vitro* activity.

To examine our hypothesis, we compared a freshly prepared mRNA-LNP sample with a representative lyophilized mRNA-LNP sample, focusing on encapsulation efficiency, structural characteristics, and *in vitro* activity. As illustrated in Figure 5a, both samples displayed comparable encapsulation efficiency, R_g, and PdI, while the lyophilized sample exhibited a larger R_h compared to the fresh sample. Previous research has suggested that larger mRNA-LNPs can maintain or enhance transfection potency (11, 24); however, the lyophilized sample demonstrated reduced *in vitro* efficacy relative to the fresh one (Figure 5b). Both fresh

and lyophilized mRNA-LNPs exhibited peaks at ~0.13 $Å^{-1}$ in SAXS characterization (Figure 5c). It is worth noting that the Gaussian peak derived from the SAXS curve of the fresh sample had greater intensity and area than that of the lyophilized sample, with similar peak widths between the two (Figure 5d). This finding suggests that the internal structure of lyophilized mRNA-LNPs is less ordered than that of the fresh sample.

To further explore mRNA distribution within the LNPs, we employed ^{31}P nuclear magnetic resonance (NMR) spectroscopy. It is known that siRNA complexed with cationic lipids within LNPs displays broad "solid-state" ^{31}P NMR resonances due to restricted mobility and large chemical shift anisotropy of the phosphate phosphorus (25, 26). In contrast, freely tumbling siRNA in an aqueous environment produces a narrow, easily detectable 31P NMR spectrum (25). We expected that fresh mRNA-LNPs would show no characteristic peak in the ^{31}P NMR spectrum, while the lyophilized sample would resemble mRNA in an aqueous solution. Consistent with this expectation, Figure 5e shows a peak at approximately -0.6 ppm in the lyophilized mRNA-LNPs, similar to that of mRNA in solution, whereas the fresh mRNA-LNPs exhibited no peak. These observations suggest that lyophilization may cause partial segregation of mRNA molecules from lipids within the LNPs, leading to a bleb morphology with distinct water and lipid compartments, as depicted in the middle inset of Figure 5e. This phase separation likely results in a less ordered internal structure, as reflected by the reduced intensity of the SAXS peak at ~0.13 $Å^{-1}$ (Figure 5c). Given the strong correlation between the intensity of the SAXS peak at ~0.13 $Å^{-1}$ and the *in vitro* activity of mRNA-LNPs (Figure 4), it appears that a more ordered internal structure is associated with higher efficacy. This conclusion aligns with prior studies on mRNA-LNPs (12, 14, 15) and is further supported by research on antisense oligonucleotide-loaded LNPs, which demonstrated that an ordered oligonucleotide-lipid phase in LNPs enhances endosomal escape and efficacy (23). Thus, the intensity of the

characteristic SAXS peak attributed to the periodic structure of mRNA and lipids may serve as a reliable indicator for optimizing mRNA-LNP formulations.

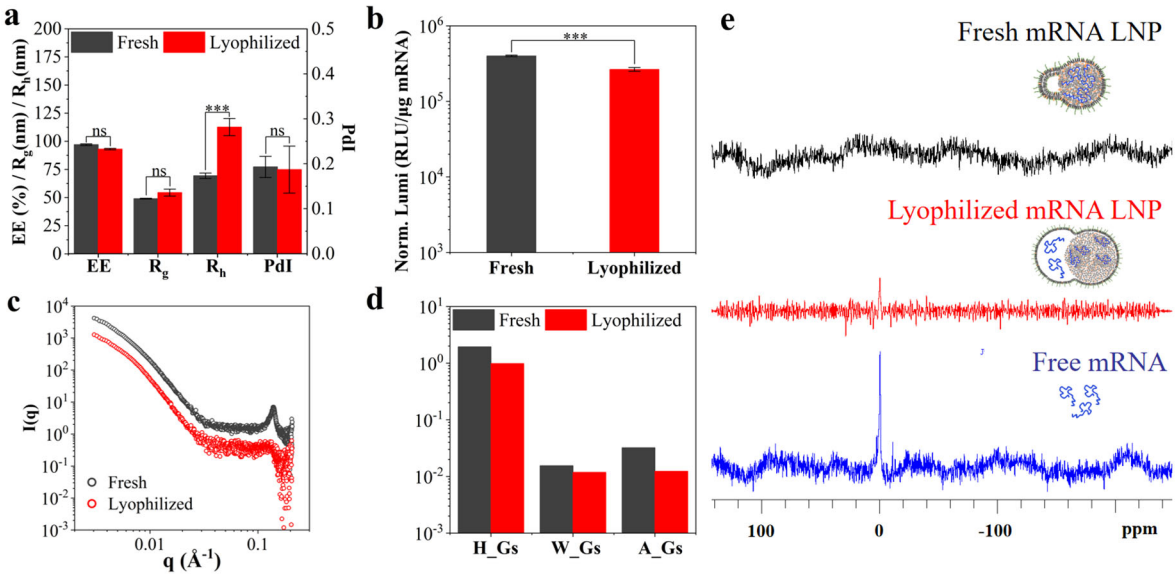

Figure 5. Comparative analysis of fresh and lyophilized mRNA-LNPs in the presence of 15% (w/v) trehalose in TB buffer. (a) A comparative evaluation of encapsulation efficiency (EE%), R_g, R_h, and PdI between fresh (black bars) and lyophilized (red bars) mRNA-LNPs. (b) A comparison of normalized luminescence intensity (Norm Lumi) between fresh (black bar) and lyophilized (red bar) mRNA-LNPs. (c) SAXS curves for fresh (black dots) and lyophilized (red dots) mRNA-LNPs, highlighting structural differences. (d) A comparison of the intensities, widths, and areas of Gaussian peaks derived from fitting the SAXS data of fresh (black bars) and lyophilized (red bars) mRNA-LNPs. (e) ^{31}P NMR spectra of free mRNA, fresh mRNA-LNPs, and lyophilized mRNA-LNPs, with upper, middle, and lower insets illustrating schematic representations of the structural organization of fresh mRNA-LNPs, lyophilized mRNA-LNPs, and free mRNA. In these schematics, blue lines represent mRNA molecules, cyan dots indicate water molecules, and other symbols denote lipid components.

Conclusion

In this study, we prepared 58 mRNA-LNPs with varied structures and *in vitro* activities by

changing their storage conditions. Structural characteristics, including R_g, R_h, PdI, R_g/R_h, and the features of the SAXS peak at ~0.13 $Å^{-1}$, were determined using DLS and SAXS techniques. Concurrently, we measured the luminescence of expressed fLuc in HEK293T cells and normalized by the transfected mRNA content encapsulated within the LNPs. Our findings indicate that normalized luminescence (Norm Lumi) exhibits minimal correlation with R_g, R_h, and R_g/R_h, suggesting that nanoparticle size and morphology are not directly associated with the *in vitro* activity of mRNA-LNPs. However, PdI, reflecting particle size distribution, shows a moderate negative correlation with *in vitro* activity, suggesting that a broad size distribution may reduce efficacy.

Additionally, the SAXS peak at ~0.13 $Å^{-1}$ was deconvoluted into two components: a Lorentz peak and a Gaussian peak, corresponding to contributions from disordered and ordered internal structures, respectively. We identified a strong correlation between the intensity of the Gaussian peak and the *in vitro* activity of mRNA-LNPs, indicating that the intensity of the characteristic SAXS peak can serve as a predictive marker for *in vitro* activity under various conditions. Moreover, the area and width of the Gaussian peak displayed moderate positive and negative correlations with activity, respectively. Based on these observations, we propose that ordered internal structures formed by mRNA and adjacent ionizable lipids may enhance the *in vitro* activity of mRNA-LNPs. Further analysis using ^{31}P NMR spectra revealed that lyophilization may cause separation of mRNA molecules from lipids within LNPs, leading to reduced Gaussian peak intensity and decreased efficacy. This finding underscores the impact of lyophilization on the stability and activity of mRNA-LNPs.

Overall, our study establishes a correlation between structure and *in vitro* activity of mRNA-LNPs using SAXS and introduces a methodology that can be applied to characterize LNPs throughout preparation, storage, and delivery stages. This workflow can be extended to identify critical formulation parameters within the vast formulation space, ultimately guiding the

optimization of LNP performance.

Acknowledgements

This work was supported by the National Natural Science Foundation of China (12204302), the Shanghai Pujiang Program (Grant No. 22PJ1406900), the Startup Fund for Young Faculty at SJTU (SFYF at SJTU), the Oceanic Interdisciplinary Program of Shanghai Jiao Tong University (Project No. SL2022MS018), the Natural Science Foundation of Shanghai (Grant No. 23ZR1431700), and the Student Innovation Center at Shanghai Jiao Tong University. We would like to thank Dr. Na Li from BL19U2 beamline of Shanghai Synchrotron Radiation Facility (SSRF) for the help with synchrotron small angle X-ray scattering measurements on No. 2022-NFPS-PT-007003.

Author contributions

Z.L. and L.H. designed and supervised the project. X.C., M.L., and F.J. prepared the samples and performed the measurements. X.C. and Z.L. analyzed the experimental data. X.C., Z.L., and L.H. wrote the manuscript.

Additional information

Correspondence and requests for materials should be addressed to judeliu@sjtu.edu.cn and hongl3liang@sjtu.edu.cn.

Competing financial interests

The authors declare no competing financial interests.

Materials and Methods

Materials. The enhanced green fluorescent protein-linked firefly luciferase (eGFP-fLuc) encoding mRNA, with a length of 2,856 nucleotides, was procured from Yaohaibio Co., Ltd. (Jiangsu, China). This mRNA was synthesized via in vitro transcription, featuring a Cap1 structure at the 5' end, pseudouridine substitution, and a 150-nucleotide poly(A) tail, with a purity exceeding 95%. The cationic ionizable lipid (CIL), heptadecan-9-yl 8-((2-hydroxyethyl)(6-oxo-6-(undecyloxy)hexyl)amino)octanoate) (SM-102, CAS: 2089251-47-6), was obtained from Sinopeg Biotechnology Co., Ltd. (Fujian, China). The 1,2-Distearoyl-sn-glycero-3-phosphocholine (DSPC, CAS: 816-94-4) was sourced from Merck (Darmstadt, Germany). Cholesterol (Chol, CAS: 57-88-5) and 1,2-Dilauryl-rac-glycero-3-methoxypolyethylene glycol 2000 (DMG-PEG2000, CAS: 160743-62-4) were supplied by Avanti Polar Lipids, Inc. (Alabaster, AL, USA). Lyoprotectants, including trehalose (Tre, CAS: 6138-23-4), sucrose (Suc, CAS: 57-50-1), maltose (Mal, CAS: 6363-53-7), and maltitol (Mai, CAS: 585-88-6), were purchased from Shaoxin Biotechnology Co., Ltd. (Shanghai, China).

LNP formulation and preparation. The mRNA was dissolved in 100 mM citrate buffer (pH 4.0) at a concentration of 72 μg/mL, serving as the aqueous phase. Four lipids were dissolved in anhydrous ethanol at a molar ratio of CIL:Chol:DSPC:DMG-PEG2000 = 50:38.5:10:1.5. Both the aqueous and ethanol phases were equilibrated to room temperature prior to use. The mRNA-LNPs were prepared using a microfluidic device (NanoGenerator Flex, Precigenome LLC, CA, USA) at a total flow rate of 4 mL/min, with an aqueous-to-ethonal phase flow rate ratio of 3:1. The mixture in the initial 5 seconds (~0.25 mL) was discarded to eliminate the scrap attributed to non-equilibrium flow rates and residual buffer in the outlet channel. The primary mRNA-LNP suspension, containing 8 mM lipid and an N:P ratio of 6:1, was immediately diluted tenfold in Tris or phosphate buffer (pH 7.4) to reduce ethanol concentration and replace the buffer. Ultra-filtration at 3000 rpm using a 100 kDa MWCO

Millipore filter was then employed to remove excess buffer. This buffer replacement was repeated to ensure that ethanol concentration in the final samples was reduced to less than 0.5%, while the mRNA-LNP was concentrated back to its initial volume prior to buffer replacement. For subsequent analyses, the mRNA-LNPs were further concentrated by ultra-filtration as needed. As a negative control, drug-free LNPs were prepared using 100 mM sodium citrate buffer (pH 4.0) as the aqueous phase, following the same method. A 30 kDa MWCO Millipore filter was used for buffer replacement and particle concentration of the drug-free LNPs.

Lyophilization protocols. To prepare mRNA-LNP samples for lyophilization, concentrated mRNA-LNP suspensions were combined with 50% (w/v) lyoprotectant in Tris- or phosphate buffer at pH 7.4, achieving final concentrations of approximately 54 µg/mL for mRNA and 10-20% (w/v) for lyoprotectants. Each 2 mL glass vial was filled with 0.5 mL of the formulated mRNA-LNP mixture and subsequently frozen at -83°C. The frozen vials were subjected to lyophilization using a laboratory freeze-dryer (Alpha 2-4 LSCplus, Martin Christ Gefriertrocknungsanlagen, Germany) equipped with a LyoCube4-8 chamber. The lyophilization protocol included a 90-minute warm-up phase to decrease the chamber pressure from 1 atm to 0.1 mbar, followed by a 36-hour primary drying phase at 0.1 mbar to remove water from the mRNA-LNP samples. A secondary drying phase at 0.01 mbar for 9 hours was then performed to further reduce residual water content and elevate the temperature to 25°C, minimizing moisture absorption due to temperature differentials. After lyophilization, vials were stoppered with rubber lids and sealed with caps equipped with sealing rings. Each vial was reconstituted with 500 µL of DEPC-treated water prior to evaluating the physicochemical properties and in vitro activity of the lyophilized mRNA-LNPs. Additionally, lyophilized samples were stored at 4°C, 25°C, and 37°C for varying durations to assess storage stability, with aqueous backup aliquots kept at -83°C in corresponding lyoprotectants.

Dynamic light scattering (DLS). The hydrodynamic radius (R_h) and polydispersity index (PdI)

of the mRNA-LNPs were determined using the NanoBrook Omni multi-angle particle size and zeta potential analyzer (Brookhaven Instruments, NH, USA). Prior to analysis, 25 μL of mRNA-LNPs was diluted with 500 μL of DEPC-treated water and transferred to a 50 μL disposable plastic cuvette (Brookhaven). Measurements were performed at a scattering angle of 90° using a 640 nm laser wavelength, with a dust filter engaged. The correlator was configured for nanoparticle analysis, and the solvent was set to water with default parameters. The refractive index of the particles was adjusted to 1.45, as ref. (10). Samples were equilibrated at 25°C for 120 seconds before measurement. The apparent hydrodynamic diameter was computed using the Einstein-Stokes equation, and the results are presented as the radius of an equivalent spherical particle.

Cryo-Electron Microscopy (Cryo-EM). The morphology of mRNA-LNPs was examined using cryogenic electron microscopy (cryo-EM). Sample preparation was carried out using a Leica EM GP2 automatic plunge freezer (Wetzlar, Germany). Briefly, 3 μL of LNP suspension, with a lipid concentration ranging from 5 to 10 mg/mL, was applied to a plasma-cleaned lacey copper grid coated with a continuous carbon film. Excess sample was removed by blotting, ensuring no damage to the carbon layer. The grids were then stored in liquid nitrogen until imaging. Cryo-EM imaging was performed on a Talos F200C G2 Microscope (Thermo Fisher Scientific, MA, USA) operated at 200 kV, and equipped with a Schottky thermal field emission electron gun. During the imaging process, the sample grids were maintained at temperatures below −170 °C. Images were captured using a FEI Ceta (4 k × 4 k) camera, and data acquisition was facilitated using the EPU and Serial EM software.

Encapsulation efficiency. The encapsulation efficiency (EE%) of mRNA-LNPs was assessed using the Quant-iT RiboGreen RNA Quantification Kit, following the manufacturer's instructions and conducted in a black 96-well plate. Briefly, 1 μL of mRNA-LNP suspension was diluted in 100 μL of Tris-EDTA (TE) buffer for measurement of free mRNA, or in TE

buffer containing 2% Triton X-100 for measurement of total mRNA. Triton X-100 disrupts the LNPs, releasing the encapsulated mRNA, which allows for its detection. Subsequently, 100 μL of a RiboGreen solution, diluted 2000-fold for free mRNA and 200-fold for total mRNA, was added to the respective wells. RiboGreen, a fluorescent dye, exhibits enhanced fluorescence upon binding to nucleic acids. Fluorescence intensity was measured at 525 nm with an excitation wavelength of 425 nm using a Spark multimode microplate reader (Tecan, Männedorf, Switzerland). Calibration curves were generated for mRNA concentrations ranging from 0 to 100 ng/mL and 0 to 2000 ng/mL, prepared by sequential dilutions and mixed with the RiboGreen solutions in the same plate as the samples. The concentrations of free and total mRNA were determined from these calibration curves and used to calculate the encapsulation efficiency (EE%) using the formula $[100 - C_{free} / C_{total} \times 100]$ %, where C_{total} represented the total mRNA concentration in the presence of 2% Triton X-100, and C_{free} was the concentration of free or unencapsulated mRNA.

***In vitro* cell transfection.** Human Embryonic Kidney 293 cells stably expressing the sheared Simian Virus 40 Large T Antigen (HEK293T) (obtained from the Chinese Academy of Sciences Shanghai Institutes for Biological Sciences Cell Resource Center, Shanghai, China) were cultured according to established protocols. The cells were maintained in high-glucose Dulbecco's Modified Eagle Medium (DMEM) (Thermo Fisher Scientific, CA, USA) supplemented with 10% fetal bovine serum (Gibco, Australia) and 1% penicillin/streptomycin. Cultures were incubated at 37 °C in a 5% CO_2 atmosphere. For transfection, cells were seeded at a density of 3×10^5 cells/mL in 24-well plates, with 500 μL per well, and allowed to adhere and proliferate for 24 hours. Transfection was carried out by adding 20 μL of mRNA-LNP suspension dropwise to the culture medium in triplicate wells, followed by a further 24-hour incubation period. mRNA expression in HEK293T cells was assessed by measuring fLuc activity using the Firefly Luciferase Reporter Gene Assay Kit (RG006, Beyotime

Biotechnology, Shanghai, China), following the manufacturer's instructions. After aspirating the culture medium, 100 μL of cell lysis buffer was added to each well. The cell lysate was centrifuged at 10,000×g for 5 minutes, and 40 μL of the supernatant was combined with 100 μL of Firefly Luciferase Assay Reagent. Luminescence was measured using a SpectraMax iD5 multi-mode microplate reader (Becton, Dickinson and Company, NJ, USA). The relative luminescence units (RLU) were normalized to the amount of encapsulated mRNA, as quantified using the Quant-iT RiboGreen RNA Quantification Kit, and are reported as normalized luminescence (Norm Lumi).

Small angle X-ray scattering (SAXS). Synchrotron small-angle X-ray scattering (SAXS) measurements were conducted at the BL19U2 beamline of the Shanghai Synchrotron Radiation Facility (SSRF), utilizing an X-ray wavelength of 0.103 nm. The experimental setup included a Pilatus 2 M detector (172 μm × 172 μm) with a resolution of 1043 × 981 pixels. The sample-to-detector distance was maintained at 5.68 meters, with the scattering vector q spanning from 0.003 $Å^{-1}$ to 0.208 $Å^{-1}$. Data acquisition involved capturing twenty consecutive two-dimensional (2D) images, each with a 0.5-second exposure time. These 2D images were subsequently integrated into one-dimensional (1D) intensity profiles using BioXTAS RAW 2.3.0 software (27). The final intensity curves were obtained by averaging the data from all 20 frames and subtracting the corresponding solvent background.

Data analysis of SAXS. The scattering curves of a particle $I(q)$ is a Fourier transform of its pair distance distribution function, $P(r)$, being related to each other by the equation (28):

$$P(r) = \frac{r^2}{2\pi^2}\int_0^\infty \frac{q^2 I(q)\sin(qr)}{qr}\,dq \qquad (1)$$

where r is the pair distance in real space, and q is the momentum transfer in reciprocal space. Furthermore, the radius of gyration (R_g) can be calculated from the $P(r)$ function using the equation (28):

$$R_g^2 = \frac{\int_0^{D_{max}} r^2 P(r) dr}{2 \int_0^{D_{max}} P(r) dr} \quad (2)$$

where D_{max} is the maximum dimension of the particle.

SAXS data for drug-free LNPs was fitted using a broad peak model in SasView (https://www.sasview.org/) with details on the fitting constraints given in the SI. The SAXS data for mRNA-LNPs was fitted using a combination of the broad peak model and one Gaussian peak. The peak position from the broad peak model were fixed, with other parameters allowed to vary, while all of the Gaussian peak parameters were allowed to vary. For all samples, the data was fitted over the q range 0.02 – 0.2 $Å^{-1}$. The areas of the broad peak and the Gaussian peak correspond to the contributions from disordered and ordered structures in the mRNA-LNP samples, respectively.

Nuclear Magnetic Resonance (NMR). The ^{31}P NMR spectra for concentrated mRNA, fresh mRNA-LNP, and lyophilized mRNA-LNP samples were acquired using a Bruker AVANCE NEO 700 MHz NMR spectrometer. This system was equipped with a 5 mm helium-cooled broadband cryo-probe and a wide-bore superconducting magnet providing a magnetic field strength of 16.4 T (700 MHz), located at Bruker BioSpin (Germany).

Statistical analysis. To assess the significance of the observed differences among groups, Analysis of Variance (ANOVA) was conducted, followed by a Dunn-Sidak post-hoc test for multiple comparisons. A significance level of $\alpha = 0.05$ was applied, and all pairwise comparisons were adjusted using the Dunn-Sidak correction within the statistical toolbox of Origin software.

Table of Content

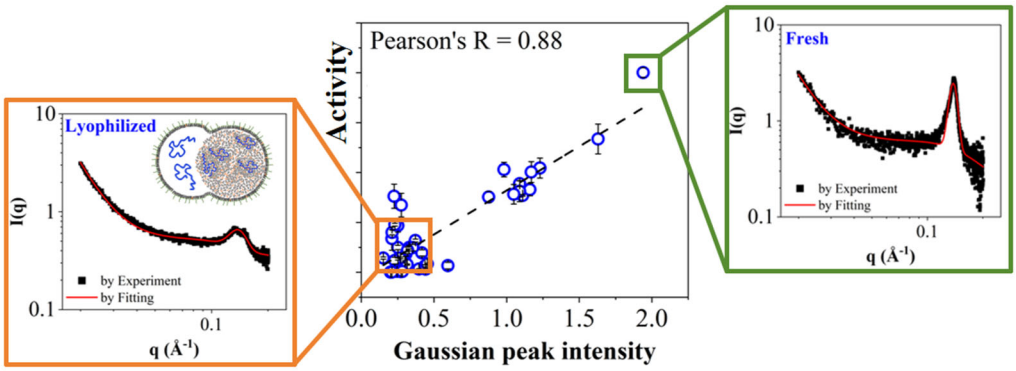

References

1. F. P. Polack, S. J. Thomas, N. Kitchin *et al.*, Safety and Efficacy of the BNT162b2 mRNA Covid-19 Vaccine. *N. Engl. J. Med.* **383**, 2603-2615 (2020).
2. L. R. Baden, H. M. El Sahly, B. Essink *et al.*, Efficacy and Safety of the mRNA-1273 SARS-CoV-2 Vaccine. *N. Engl. J. Med.* **384**, 403-416 (2020).
3. X. Hou, T. Zaks, R. Langer, Y. Dong, Lipid nanoparticles for mRNA delivery. *Nature Reviews Materials* **6**, 1078-1094 (2021).
4. R. Tenchov, R. Bird, A. E. Curtze, Q. Zhou, Lipid Nanoparticles—From Liposomes to mRNA Vaccine Delivery, a Landscape of Research Diversity and Advancement. *ACS Nano* **15**, 16982-17015 (2021).
5. A. J. Barbier, A. Y. Jiang, P. Zhang, R. Wooster, D. G. Anderson, The clinical progress of mRNA vaccines and immunotherapies. *Nat. Biotechnol.* **40**, 840-854 (2022).
6. Y. Weng, C. Li, T. Yang *et al.*, The challenge and prospect of mRNA therapeutics landscape. *Biotechnol. Adv.* **40**, 107534 (2020).
7. E. Wilson, J. Goswami, H. Baqui Abdullah *et al.*, Efficacy and Safety of an mRNA-Based RSV PreF Vaccine in Older Adults. *N. Engl. J. Med.* **389**, 2233-2244 (2023).
8. M. H. Y. Cheng, J. Leung, Y. Zhang *et al.*, Induction of Bleb Structures in Lipid Nanoparticle Formulations of mRNA Leads to Improved Transfection Potency. *Adv. Mater.* **35**, 2303370 (2023).
9. S. Patel, N. Ashwanikumar, E. Robinson *et al.*, Naturally-occurring cholesterol analogues in lipid nanoparticles induce polymorphic shape and enhance intracellular delivery of mRNA. *Nat. Commun.* **11**, 983 (2020).
10. M. Yanez Arteta, T. Kjellman, S. Bartesaghi *et al.*, Successful reprogramming of cellular protein production through mRNA delivered by functionalized lipid nanoparticles. *Proc. Natl. Acad. Sci. U. S. A.* **115**, E3351-E3360 (2018).
11. L. Cui, M. R. Hunter, S. Sonzini *et al.*, Mechanistic Studies of an Automated Lipid Nanoparticle Reveal Critical Pharmaceutical Properties Associated with Enhanced mRNA Functional Delivery In Vitro and In Vivo. *Small* **18**, 2105832 (2022).
12. H. Yu, J. Iscaro, B. Dyett *et al.*, Inverse Cubic and Hexagonal Mesophase Evolution within Ionizable Lipid Nanoparticles Correlates with mRNA Transfection in Macrophages. *J. Am. Chem. Soc.* **145**, 24765-24774 (2023).
13. H. Yu, A. Angelova, B. Angelov *et al.*, Real-Time pH-Dependent Self-Assembly of Ionisable Lipids from COVID-19 Vaccines and In Situ Nucleic Acid Complexation. *Angewandte Chemie International Edition* **62**, e202304977 (2023).
14. L. Zheng, S. R. Bandara, Z. Tan, C. Leal, Lipid nanoparticle topology regulates endosomal escape and delivery of RNA to the cytoplasm. *Proc. Natl. Acad. Sci. U. S. A.* **120**, e2301067120 (2023).
15. J. Philipp, A. Dabkowska, A. Reiser *et al.*, pH-dependent structural transitions in cationic ionizable lipid mesophases are critical for lipid nanoparticle function. *Proc. Natl. Acad. Sci. U. S. A.* **120**, e2310491120 (2023).
16. F. Sebastiani, M. Yanez Arteta, M. Lerche *et al.*, Apolipoprotein E Binding Drives Structural and Compositional Rearrangement of mRNA-Containing Lipid Nanoparticles. *ACS Nano* **15**, 6709-6722 (2021).
17. M. L. Brader, S. J. Williams, J. M. Banks *et al.*, Encapsulation state of messenger RNA inside lipid nanoparticles. *Biophys. J.* **120**, 2766-2770 (2021).
18. J. Gilbert, F. Sebastiani, M. Y. Arteta *et al.*, Evolution of the structure of lipid nanoparticles for nucleic acid delivery: From in situ studies of formulation to colloidal stability. *J. Colloid Interface Sci.* **660**, 66-76 (2024).

19. J. L. Thelen, W. Leite, V. S. Urban *et al.*, Morphological Characterization of Self-Amplifying mRNA Lipid Nanoparticles. *ACS Nano* **18**, 1464-1476 (2024).
20. Y. Li, C. Ma, Z. Han *et al.*, Morphology evolution of lipid nanoparticle discovered by small angle neutron scattering. *Giant* **20**, 100329 (2024).
21. P. Zhao, X. Hou, J. Yan *et al.*, Long-term storage of lipid-like nanoparticles for mRNA delivery. *Bioactive Materials* **5**, 358-363 (2020).
22. S. S. Nogueira, A. Schlegel, K. Maxeiner *et al.*, Polysarcosine-Functionalized Lipid Nanoparticles for Therapeutic mRNA Delivery. *ACS Applied Nano Materials* **3**, 10634-10645 (2020).
23. M. Hammel, Y. Fan, A. Sarode *et al.*, Correlating the Structure and Gene Silencing Activity of Oligonucleotide-Loaded Lipid Nanoparticles Using Small-Angle X-ray Scattering. *ACS Nano* **17**, 11454-11465 (2023).
24. K. J. Hassett, J. Higgins, A. Woods *et al.*, Impact of lipid nanoparticle size on mRNA vaccine immunogenicity. *Journal of Controlled Release* **335**, 237-246 (2021).
25. A. K. K. Leung, I. M. Hafez, S. Baoukina *et al.*, Lipid Nanoparticles Containing siRNA Synthesized by Microfluidic Mixing Exhibit an Electron-Dense Nanostructured Core. *The Journal of Physical Chemistry C* **116**, 18440-18450 (2012).
26. J. A. DiVerdi, S. J. Opella, R. I. Ma, N. R. Kallenbach, N. C. Seeman, 31P NMR of DNA in eukaryotic chromosomal complexes. *Biochem. Biophys. Res. Commun.* **102**, 885-890 (1981).
27. J. Hopkins, BioXTAS RAW 2: new developments for a free open-source program for small-angle scattering data reduction and analysis. *J. Appl. Crystallogr.* **57**, 194-208 (2024).
28. I. S. Dmitri, H. J. K. Michel, Small-angle scattering studies of biological macromolecules in solution. *Reports on Progress in Physics* **66**, 1735 (2003).

Revealing a Correlation between Structure and *in vitro* Activity of mRNA Lipid Nanoparticles

Xiaoxia Chen[1,2], Mengrong Li[1,2], Fan Jiang[1,2], Liang Hong[1,2,3,4,5,*], and Zhuo Liu[2,3,4,5,*]

[1]School of Physics and Astronomy, Shanghai Jiao Tong University, Shanghai 200240, China.

[2]Institute of Natural Sciences, Shanghai Jiao Tong University, Shanghai 200240, China.

[3]Shanghai National Centre for Applied Mathematics (SJTU Center), MOE-LSC, Shanghai Jiao Tong University, Shanghai 200240, China.

[4]Zhangjiang Institute for Advanced Study, Shanghai Jiao Tong University, Shanghai 201203, China.

[5]Shanghai Artificial Intelligence Laboratory, Shanghai 200232, China.

*e-mail: judeliu@sjtu.edu.cn and hongl3liang@sjtu.edu.cn

Table S1. Detailed sample information for mRNA-LNPs.

Sample Name	Buffer	Lyoprotectant	Sample state	Temperature	Storage period/weeks
TB_10Tre_Fresh	TB	10% Trehalose	Fresh	/	/
TB_10Tre_FZ	TB	10% Trehalose	Frozen	-83 ºC	24
TB_15Tre_FZ	TB	15% Trehalose	Frozen	-83 ºC	24
TB_20Tre_FZ	TB	20% Trehalose	Frozen	-83 ºC	24
TB_10Suc_FZ	TB	10% Sucrose	Frozen	-83 ºC	24
TB_15Suc_FZ	TB	15% Sucrose	Frozen	-83 ºC	24
TB_20Suc_FZ	TB	20% Sucrose	Frozen	-83 ºC	24
TB_10Mal_FZ	TB	10% Maltose	Frozen	-83 ºC	24
TB_15Mal_FZ	TB	15% Maltose	Frozen	-83 ºC	24
TB_20Mal_FZ	TB	20% Maltose	Frozen	-83 ºC	24
TB_10Mai_FZ	TB	10% Maltitol	Frozen	-83 ºC	24
TB_15Mai_FZ	TB	15% Maltitol	Frozen	-83 ºC	24
TB_20Mai_FZ	TB	20% Maltitol	Frozen	-83 ºC	24
PB_10Tre_FZ	PB	10% Trehalose	Frozen	-83 ºC	24
PB_15Tre_FZ	PB	15% Trehalose	Frozen	-83 ºC	24
PB_20Tre_FZ	PB	20% Trehalose	Frozen	-83 ºC	24
PB_10Suc_FZ	PB	10% Sucrose	Frozen	-83 ºC	24
PB_15Suc_FZ	PB	15% Sucrose	Frozen	-83 ºC	24
PB_20Suc_FZ	PB	20% Sucrose	Frozen	-83 ºC	24
PB_10Mal_FZ	PB	10% Maltose	Frozen	-83 ºC	24
PB_15Mal_FZ	PB	15% Maltose	Frozen	-83 ºC	24
PB_20Mal_FZ	PB	20% Maltose	Frozen	-83 ºC	24
PB_10Mai_FZ	PB	10% Maltitol	Frozen	-83 ºC	24
PB_15Mai_FZ	PB	15% Maltitol	Frozen	-83 ºC	24
PB_20Mai_FZ	PB	20% Maltitol	Frozen	-83 ºC	24
TB_10Tre_FD	TB	10% Trehalose	Lyophilized	/	/
TB_15Tre_FD	TB	15% Trehalose	Lyophilized	/	/
TB_20Tre_FD	TB	20% Trehalose	Lyophilized	/	/
TB_10Suc_FD	TB	10% Sucrose	Lyophilized	/	/
TB_15Suc_FD	TB	15% Sucrose	Lyophilized	/	/
TB_20Suc_FD	TB	20% Sucrose	Lyophilized	/	/
TB_10Mal_FD	TB	10% Maltose	Lyophilized	/	/
TB_15Mal_FD	TB	15% Maltose	Lyophilized	/	/
TB_20Mal_FD	TB	20% Maltose	Lyophilized	/	/
TB_10Mai_FD	TB	10% Maltitol	Lyophilized	/	/
TB_15Mai_FD	TB	15% Maltitol	Lyophilized	/	/
TB_20Mai_FD	TB	20% Maltitol	Lyophilized	/	/
PB_10Tre_FD	PB	10% Trehalose	Lyophilized	/	/
PB_15Tre_FD	PB	15% Trehalose	Lyophilized	/	/
PB_20Tre_FD	PB	20% Trehalose	Lyophilized	/	/
PB_10Suc_FD	PB	10% Sucrose	Lyophilized	/	/
PB_15Suc_FD	PB	15% Sucrose	Lyophilized	/	/
PB_20Suc_FD	PB	20% Sucrose	Lyophilized	/	/
PB_10Mal_FD	PB	10% Maltose	Lyophilized	/	/
PB_15Mal_FD	PB	15% Maltose	Lyophilized	/	/

Table S1. (Continued)

Sample Name	Buffer	Lyoprotectant	Sample state	Temperature	Storage period/weeks
PB_20Mal_FD	PB	20% Maltose	Lyophilized	/	/
PB_10Mai_FD	PB	10% Maltitol	Lyophilized	/	/
PB_15Mai_FD	PB	15% Maltitol	Lyophilized	/	/
PB_20Mai_FD	PB	20% Maltitol	Lyophilized	/	/
-18FD_24w	TB	15% Trehalose	Lyophilized	-18 ºC	24
4FD_4w	TB	15% Trehalose	Lyophilized	4 ºC	4
4FD_12w	TB	15% Trehalose	Lyophilized	4 ºC	12
4FD_20w	TB	15% Trehalose	Lyophilized	4 ºC	20
25FD_4w	TB	15% Trehalose	Lyophilized	25 ºC	4
25FD_12w	TB	15% Trehalose	Lyophilized	25 ºC	12
25FD_20w	TB	15% Trehalose	Lyophilized	25 ºC	20
37FD_4w	TB	15% Trehalose	Lyophilized	37 ºC	4
37FD_8w	TB	15% Trehalose	Lyophilized	37 ºC	8

TB and PB correspond to Tris and phosphate buffer, respectively.

Data fitting for SAXS measurements of drug-free LNPs and mRNA-LNPs.

The SAXS data for drug-free LNPs were fitted using the broad peak model implemented in SASView (https://www.sasview.org/), with all fitting parameters permitted to vary. The resulting parameters are detailed in Table S2. For the mRNA-LNPs, the SAXS data were fitted using a combination of the broad peak model and a Gaussian peak. The broad peak position and Porod exponent were fixed based on the drug-free LNP fitting results, while the other parameters were variable, along with all parameters of the Gaussian peak. Figure S1 illustrates the fitting curves for 40 mRNA-LNP samples, with the corresponding fitting parameters provided in Table S3.

Table S2. Fitting parameters for the SAXS data of drug-free LNPs with the broad peak model.

Parameters	Value
Porod scale	1.88×10^{-5}
Porod exponent	3.696
Lorentz scale	2.647
Lorentz length	13.211
Peak position	0.06964

Table S3. Parameters of broad peak and Gaussian peak employed to fit the SAXS data for mRNA LNPs.

Sample name	Board peak		Gaussian Peak		
	Porod scale	Lorentz scale	Scale	Peak center	σ
TB_10Tre_Fresh	1.312E-06	0.3016	1.9436	0.1382	6.592E-03
TB_10Tre_FZ	2.480E-06	0.1886	0.3078	0.1234	2.272E-02
TB_15Tre_FZ	1.399E-06	0.3451	0.2990	0.1276	1.782E-02
TB_20Tre_FZ	2.600E-06	0.2728	0.3156	0.1276	1.951E-02
TB_10Suc_FZ	2.044E-06	0.3249	0.3972	0.1314	1.855E-02
TB_15Suc_FZ	3.163E-06	0.3641	0.4383	0.1339	1.801E-02
TB_20Suc_FZ	3.818E-06	0.3826	0.4419	0.1356	1.475E-02
TB_10Mal_FZ	1.308E-06	0.3668	0.2508	0.1342	1.590E-02
TB_15Mal_FZ	1.845E-06	0.4958	0.4166	0.1361	1.397E-02
TB_20Mal_FZ	2.638E-06	0.5347	0.4536	0.1374	1.356E-02
TB_10Mai_FZ	1.255E-07	0.5000	0.2514	0.1307	1.107E-02
TB_15Mai_FZ	9.352E-07	0.5000	0.2699	0.1319	1.133E-02
TB_20Mai_FZ	1.680E-06	0.5000	0.3286	0.1359	1.071E-02
PB_20Suc_FZ	2.969E-06	0.5000	0.1509	0.1355	6.592E-03
PB_10Mal_FZ	1.584E-06	0.5436	0.2457	0.1239	1.827E-02
PB_15Mal_FZ	9.347E-07	0.4828	0.2727	0.1280	1.619E-02
PB_20Mal_FZ	1.026E-06	0.4463	0.2815	0.1323	1.508E-02
TB_10Tre_FD	1.762E-07	0.3561	0.9815	0.1357	1.499E-02
TB_15Tre_FD	9.288E-07	0.9413	1.6314	0.1376	5.004E-03
TB_20Tre_FD	2.181E-06	0.5000	0.2110	0.1295	6.541E-03
TB_10Suc_FD	9.606E-07	0.3816	0.3721	0.1320	1.686E-02
TB_15Suc_FD	1.564E-06	0.1766	0.3542	0.1344	1.531E-02
TB_20Suc_FD	1.586E-06	0.2646	0.3190	0.1387	2.006E-02
TB_10Mal_FD	3.490E-07	0.5952	0.2260	0.1307	2.006E-02
TB_15Mal_FD	1.014E-06	0.2318	0.2511	0.1330	1.961E-02
TB_20Mal_FD	1.555E-06	0.1900	0.2747	0.1359	1.311E-02
TB_10Mai_FD	3.311E-73	0.7392	0.2300	0.1287	1.227E-02
TB_15Mai_FD	3.771E-07	0.6249	0.2122	0.1289	1.127E-02
TB_20Mai_FD	1.090E-06	0.2036	0.2310	0.1313	1.397E-02
PB_15Mal_FD	3.171E-07	0.3605	0.2018	0.1268	1.149E-02
PB_20Mal_FD	8.572E-07	0.5043	0.2109	0.1300	1.514E-02
-18FD_24w	1.999E-06	0.5142	0.5964	0.1339	2.030E-02
4FD_4w	8.137E-06	0.9352	1.2282	0.1378	1.764E-02
4FD_12w	7.925E-06	0.8720	1.1743	0.1375	1.721E-02
4FD_20w	7.113E-06	0.7868	1.1146	0.1371	1.708E-02
25FD_4w	6.282E-06	0.8659	1.0947	0.1383	1.412E-02
25FD_12w	7.203E-06	0.9030	1.1641	0.1386	1.387E-02
25FD_20w	5.680E-06	0.8414	1.0941	0.1364	1.483E-02
37FD_4w	4.235E-06	0.8201	1.0496	0.1368	1.429E-02
37FD_8w	4.645E-06	0.7741	0.8774	0.1365	1.494E-02

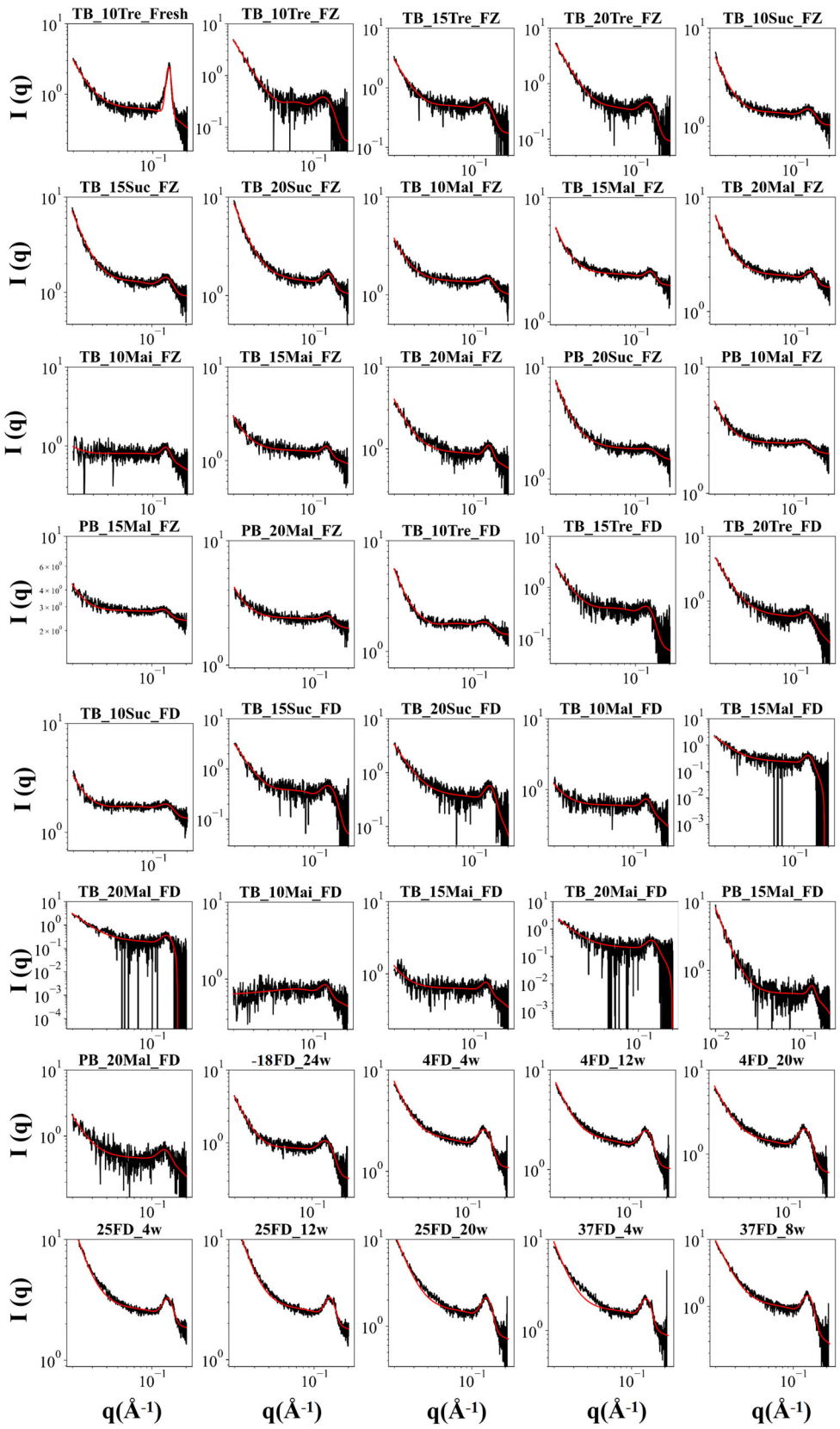

Figure S1. All peaks present in the SAXS data for various mRNA-LNPs were fitted with a broad peak model plus a Gaussian peak in a q range from 0.02 $Å^{-1}$ to 0.2 $Å^{-1}$.

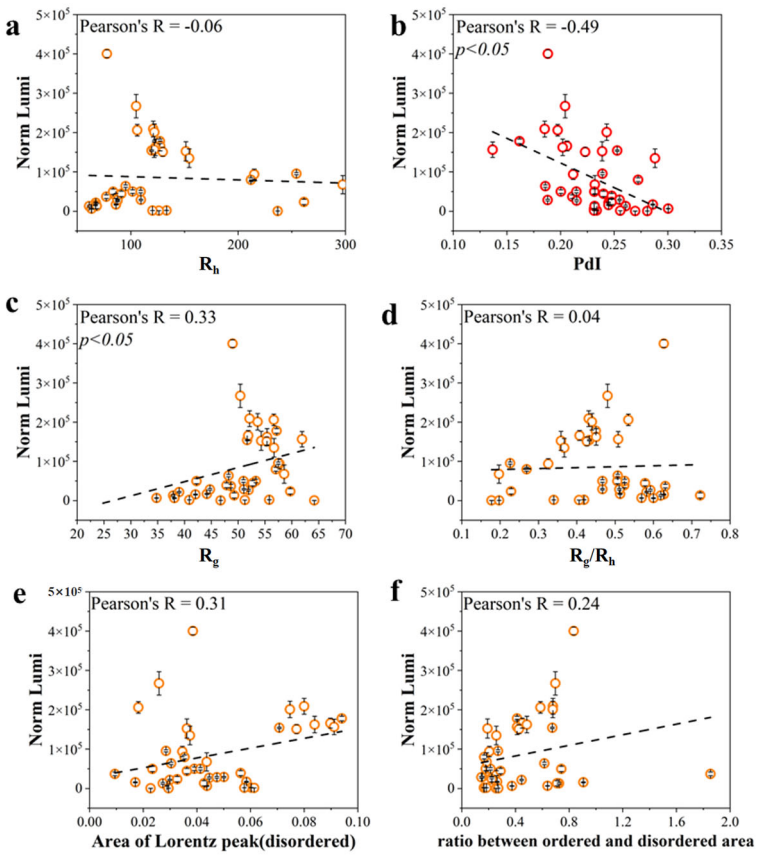

Figure S2. Correlation between Norm Lumi of mRNA-LNPs with the (a) R_h, (b) PdI, (c) R_g, (d) R_g/R_h, (e) area of Lorentz peak obtained by fitting the SAXS curves, and (f) ratio between the areas of Gaussian peak and Lorentz peak. Notably, the correlation analysis was based on 40 mRNA-LNP samples exhibiting an evident scattering peak at ~0.13 $Å^{-1}$ in SAXS.